Evolutions of nearly maximally spinning black hole binaries using the moving puncture approach

Yosef Zlochower,[1] James Healy,[1] Carlos O. Lousto,[1] and Ian Ruchlin[2]

[1]*Center for Computational Relativity and Gravitation, School of Mathematical Sciences,*
Rochester Institute of Technology, 85 Lomb Memorial Drive, Rochester, New York 14623, USA
[2]*Department of Mathematics, West Virginia University, Morgantown, West Virginia 26506, USA*

We demonstrate that numerical relativity codes based on the *"moving punctures"* formalism are capable of evolving nearly maximally spinning black hole binaries. We compare a new evolution of an equal-mass, aligned-spin binary with dimensionless spin $\chi = 0.99$ using puncture-based data with recent simulations of the SXS Collaboration. We find that the overlap of our new waveform with the published results of the SXS Collaboration is larger than 0.999. To generate our new waveform, we use the recently introduced HiSpID puncture data, the CCZ4 evolution system, and a modified lapse condition that helps keep the horizon radii reasonably large.

I. INTRODUCTION

Since the breakthroughs in numerical relativity of 2005 [1–3], it is possible to accurately simulate moderate-mass-ratio and moderate-spin black-hole binaries. State of the art numerical relativity codes now routinely evolve binaries with mass ratios as small as $q \lesssim 1/20$ [4–9] and are pushing towards much smaller mass ratios. Indeed, there have been several explorations of $q = 1/100$ binaries [6,7].

However, when it comes to highly spinning binaries, prior to the work of [10] of the SXS Collaboration [11], it was not even possible to construct initial data for binaries with spins larger than ~0.93 [12]. This limitation was due to the use of conformally flat initial data. Conformal flatness is a convenient assumption because the Einstein constraint system takes on particularly simple forms. Indeed, using the puncture approach, the momentum constraints can be solved exactly using the Bowen-York ansatz [13]. There were several attempts to increase the spin of the black hole, while still preserving conformal flatness [14,15], but these introduced negligible improvements. Lovelace *et al.* [10] were able to overcome these limitations by choosing the initial data to be a superposition of conformally Kerr black holes in the Kerr-Schild gauge. Using these new data, they were soon able to evolve binaries with spins as large as 0.97 [16] and, later, spins as high as 0.994 [17].

While spins of 0.92 may seem reasonably close to 1, the scale is misleading. The amount of rotational energy in a black hole with spin 0.9 is only 52% of the maximum. Furthermore, particle limit and perturbative calculations show even more extreme differences between spins of 1 and spins only slightly smaller. For example, Yang *et al.* [18] studied an analog to turbulence in black-hole perturbation theory. For spins close to 1, there is an inverse energy cascade from higher azimuthal (*m*) modes to lower ones for ℓ modes that obey $\epsilon = |1 - \chi| \lesssim \ell^{-2}$. This gives hints that a more useful measure of the spin is actually $1/\epsilon$. Similarly, both the analysis of Kerr geodesics [19,20], and particle-limit calculations of recoils [21,22], indicates that the dynamics of nearly extremal-spin black holes cannot be elucidated with any degree of certainty using lower spin simulations.

Another area of interest is the use of numerical relativity waveforms in the detection and parameter estimation of gravitational wave signals as observed by LIGO and other detectors [23]. This important region of parameter space with highly spinning binaries is currently poorly covered and will benefit from new and accurate simulations.

Recently, we introduced a version of highly spinning initial data, also based on the superposition of two Kerr black holes [24,25], but this time in a puncture gauge. The main differences between the two approaches is how easily the latter can be incorporated into moving-punctures codes. In Ref. [24], we were able to evolve an equal-mass binary with aligned spins, and spin magnitudes of $\chi = 0.95$, using this new data and compare with the results of the Lovelace *et al.*

Prior to our work, Hannam *et al.* [26] considered the case of nonboosted, highly spinning black holes. Similar to what we see here, they found that removing the conformally flat ansatz greatly reduces the amount of unphysical radiation.

In this paper, we show the results of a simulation of an equal-mass binary with aligned spins of $\chi = 0.99$. We compare the $(\ell = 2, m = 2)$ and $(\ell = 3, m = 2)$ modes of the waveform with those previously published by the SXS Collaboration in [17]. This comparison allows us to assess the errors in these waveforms and to gain confidence about reaching the required accuracy for use in gravitational wave astronomy.

We use the following standard conventions throughout this paper. In all cases, we use geometric units where $G = 1$ and $c = 1$. Latin letters ($i, j, \ldots$) represent spatial indices.

Spatial 3-metrics are denoted by γ_{ij} and extrinsic curvatures by K_{ij}. The trace-free part of the extrinsic curvature is denoted by A_{ij}. A tilde indicates a conformally related quantity. Thus $\gamma_{ij} = \psi^4 \tilde{\gamma}_{ij}$ and $A_{ij} = \psi^{-2} \tilde{A}_{ij}$, where ψ is some conformal factor. We denote the covariant derivative associated with γ_{ij} by D_i and the covariant derivative associated with $\tilde{\gamma}_{ij}$ by $\tilde{D}_i$. A lapse function is denoted by α, while a shift vector by β^i.

This paper is organized as follows. In Sec. II A, we provide a brief overview of how the initial data are constructed. In Sec. II B, we describe the numerical techniques used to evolve these data. In Sec. III, we compare the new HISPID waveform with a similar SXS waveform. In Sec. III A, we analyze the various diagnostics to determine the accuracy of the simulation. Finally, in Sec. IV, we discuss our results.

II. NUMERICAL TECHNIQUES

A. Initial data

We construct initial data for a black-hole binary with individual spins $\chi_{1,2} = 0.99$ using the HISPID code [24,25]. The HISPID code solves the four Einstein constraint equations using the conformal transverse traceless decomposition [27–30]. In this approach, the spatial metric γ_{ij} and extrinsic curvature K_{ij} are given by

$$\gamma_{ij} = \psi^4 \tilde{\gamma}_{ij}, \tag{1}$$

$$K_{ij} = \psi^{-2} \tilde{A}_{ij} + \frac{1}{3} K \gamma_{ij}, \tag{2}$$

$$\tilde{A}_{ij} = \tilde{M}_{ij} + (\tilde{\mathbb{L}} b)_{ij}, \tag{3}$$

where the conformal metric $\tilde{\gamma}_{ij}$, the trace of the extrinsic curvature K, and the trace-free tensor $\tilde{M}_{ij}$ are free data. The Einstein constraints then become a set of four coupled elliptical equations for the scalar field $u = \psi - \psi_0$ and components of the spatial vector b^i (ψ_0 is a singular function specified analytically). The resulting elliptical equations are solved using an extension to the TWOPUNCTURES [31] thorn.

The free data are chosen by superimposing two boosted Kerr black holes, as described in more detail in [24]. The superposition has the form

$$\tilde{\gamma}_{ij} = \tilde{\gamma}_{ij}^{(+)} + \tilde{\gamma}_{ij}^{(-)} - \delta_{ij}, \tag{4}$$

$$K = K^{(+)} + K^{(-)}, \tag{5}$$

$$M_{ij} = [\tilde{A}_{ij}^{(+)} + \tilde{A}_{ij}^{(-)}]^{\mathbf{TF}}, \tag{6}$$

$$\psi_0 = \psi_{(+)} + \psi_{(-)} - 1, \tag{7}$$

where $(+)$ and $(-)$ refer to the two black holes, $\tilde{\gamma}_{ij}^{(\pm)}$ and $\tilde{A}_{ij}$ are the conformal metric and trace-free extrinsic curvatures for a boosted and rotated Kerr black hole, $K^{(\pm)}$ is the mean curvature, and the conformal factor $\psi_{(\pm)}$ is chosen such that $\psi_{(\pm)} = \sqrt[12]{\det(\gamma_{ij}^{(\pm)})}$ (where $\gamma_{ij}^{(\pm)}$ is the physical metric from a boosted and rotated Kerr black hole).

To get $\tilde{\gamma}_{ij}^{(\pm)}$, etc., we start with Kerr black holes in quasi-isotropic (QI) coordinates and perform a fisheye (FE) radial coordinate transformation (where $r_{QI} = 0$ is the location of the puncture),

$$r_{QI} = r_{FE}[1 - A_{FE} \exp(-r_{FE}^2/s_{FE}^2)], \tag{8}$$

where r_{FE} is the fisheye radial coordinate, r_{QI} is the original QI radial coordinate, and A_{FE} and s_{FE} are parameters. These coordinates have the property that at large r_{FE}, $r_{QI} \approx r_{FE}$, and at small r_{FE}, $dr_{QI} = (1 - A)dr_{FE}$ (i.e., $dr_{QI} < dr_{FE}$). The FE transformation is needed because it expands the horizon size from $r_h \approx 0.035$ to $r_h \approx 0.5$. We then transform the metric to Cartesian-like coordinates of the form $x = r \sin\theta \cos\phi$, $y = r \sin\theta \sin\phi$, $z = r \cos\theta$, where $r = r_{FE}$. We then perform a Lorentz-like boost on this metric and, in the case of nonaligned spins, a rotation. The resulting 4-metric is then decomposed into a spatial metric γ_{ij} and extrinsic curvature K_{ij}.

We use the g attenuation described in [24] to modify both the metric and elliptical equations inside the horizons. We briefly summarize the procedure here. The modified Hamiltonian and momentum constraint equations for the correction functions u and b^i are

$$\tilde{D}^2 u - g\frac{\psi \tilde{R}}{8} - g\frac{\psi^5 K^2}{12} + g\frac{\tilde{A}_{ij}\tilde{A}^{ij}}{8\psi^7} + g\tilde{D}^2(\psi_{(+)} + \psi_{(-)}) = 0, \tag{9a}$$

$$\tilde{\Delta}_{\mathbb{L}} b^i + g\tilde{D}_j \tilde{M}^{ij} - g\frac{2}{3}\psi^6 \tilde{\gamma}^{ij}\tilde{D}_j K = 0, \tag{9b}$$

where $\tilde{\Delta}_{\mathbb{L}} b^i \equiv \tilde{D}_j(\tilde{\mathbb{L}} b)^{ij}$ is the vector Laplacian and $\tilde{R}$ is the scalar curvature associated with $\tilde{\gamma}_{ij}$, and where the attenuation function g takes the form

$$g = g_+ \times g_-,$$

$$g_{\pm} = \begin{cases} 1 & \text{if } r_{\pm} > r_{max} \\ 0 & \text{if } r_{\pm} < r_{min} , \\ \mathcal{G}(r_{\pm}) & \text{otherwise,} \end{cases}$$

$$\mathcal{G}(r_{\pm}) = \frac{1}{2}\left[1 + \tanh\left(\tan\left[\frac{\pi}{2}\left(-1 + 2\frac{r_{\pm} - r_{min}}{r_{max} - r_{min}}\right)\right]\right)\right],$$

$r_{\pm}$ is the coordinate distance to puncture $(+)$ or $(-)$, and the parameters $r_{min} < r_{max}$ are chosen to be within the horizon. In addition, we attenuate the background metric itself when calculating the $\tilde{D}^2 u$ and $\tilde{\Delta}_{\mathbb{L}} b^i$. To do this, we take

$$\tilde{\gamma}_{ij} \rightarrow \delta_{ij} + g(\tilde{\gamma}_{ij} - \delta_{ij}), \tag{10}$$

$$\tilde{\Gamma}^k_{ij} \rightarrow g\tilde{\Gamma}^k_{ij}. \tag{11}$$

Note that the modified $\tilde{\Gamma}^k_{ij}$ is not consistent with the modified $\tilde{\gamma}_{ij}$. There is no advantage to making them consistent because the constraints will be violated in the attenuation zone regardless. By modifying the metric in this way, we can ensure that the elliptical system has exactly the form of the flat space Poisson system in the vicinity of the punctures.

Finally, far from the holes, we attenuate $\tilde{\gamma}_{ij}$, K, and ψ_0. This is achieved by consistently changing the metric fields and their derivatives so that

$$\tilde{\gamma}^{(\pm)}_{ij} \rightarrow f(r_\pm)(\tilde{\gamma}^{(\pm)}_{ij} - \delta_{ij}) + \delta_{ij}, \tag{12}$$

$$K^{(\pm)} \rightarrow f(r_\pm)K^{(\pm)}, \tag{13}$$

$$(\psi_{(\pm)} - 1) \rightarrow f(r_\pm)(\psi_{(\pm)} - 1), \tag{14}$$

where $f(r) = \exp(-r^4/s^4_{\text{far}})$ and $r_\pm$ is the coordinate distance to puncture $(+)$ or $(-)$.

For compatibility with the original TwoPunctures code, we chose to set up HiSpID so that the parameters of the binary are specified in terms of momenta and spins of the two holes. However, unlike for Bowen-York data, the values specified are only approximate, as the solution vector b^i can modify both of these. In practice, we find that the spins are modified by only a trivial amount while orbital angular momentum is reduced significantly. We compensate for this by choosing larger momentum parameters than those predicted by simple quasicircular conditions would imply [32]. All parameters for the $\chi = 0.99$ run are given in Table I. The quantity r_H in the table is the polar coordinate radius (which is the smallest radius on each horizon). As this is gauge dependent, it can change arbitrarily during the evolution. However, large changes are generally undesirable. The size of r_H is also directly related to the number of refinement levels required, and therefore to the computational cost. An ideal gauge would have r_H settle to a moderate value and remain there. The initial size of the horizon is chosen to be large in order to speed up the convergence of the initial data solver (this is due to the scale set by the g attenuation discussed above). However, the gauge conditions we use quickly drive r_H towards smaller values. We note that in quasi-isotropic coordinates, the coordinate radius of a maximally spinning black hole is zero.

B. Evolution

We evolve black hole binary initial data sets using the LazEv [33] implementation of the moving punctures approach for the conformal and covariant formulation of the Z4 (CCZ4) system (Ref. [34]) which includes stronger

TABLE I. Initial data parameters for a $\chi = 0.99$ highly spinning binary. The two spins are given by $\vec{S}_{1,2} = (0, 0, S)$ and the two momenta are $P_{1,2} = \pm(0, P, 0)$. The parameter $\mathcal{M}$ is the mass of the two black holes. Unlike for Bowen-York data, the momenta and spins cannot be specified exactly. However, the mass $\mathcal{M}$ is very close to the measured horizon mass m_H. Quantities denoted by "init" were measured at $t = 0$, while quantities denoted by "equi" are averaged over the several orbits. A_{FE}, s_{FE}, r_{min}, r_{max}, and s_{far} are attenuation parameters. m_H, S, χ are masses, spin angular momenta, and dimensionless spins, respectively, of the two black holes. M_{rem} and χ_{rem} are the remnant mass and dimensionless spin. The quantity r_H is the polar radius of the horizons. Finally, M_{ADM} and J_{ADM} are the ADM masses and spins.

$\mathcal{M}/M = 0.505570$	$P/M = 0.09675$
$S/M^2 = 0.253045$	$A_{\text{FE}} = 0.99$
$s_{\text{FE}} = 1.7$	$r_{\text{min}} = 0.01$
$r_{\text{max}} = 0.40$	$s_{\text{far}} = 10$
$J_{\text{ADM}}/M^2 = 1.42621$	$M_{\text{ADM}}/M = 0.99998$
$m_{H\text{init}}/M = 0.50555$	$m_{H\text{ equi}}/M = 0.5072 \pm 0.0004$
$S_{\text{init}}/M^2 = 0.2529$	$S_{\text{equi}}/M^2 = 0.2547 \pm 0.0004$
$\chi_{\text{init}} = 0.9897$	$\chi_{\text{equi}} = 0.9903 \pm 0.0002$
$r_{H\text{ init}}/M = 0.44$	$r_{H\text{ equi}}/M = 0.081 \pm 0.001$
$M_{\text{rem}}/M = 0.898 \pm 0.001$	$\chi_{\text{rem}} = 0.949 \pm 0.001$

damping of the constraint violations than the standard BSSNOK [35–37] system. For the run presented here, we use centered, eighth-order accurate finite differencing in space [38] and a fourth-order Runge-Kutta time integrator. Our code uses the Cactus/ EinsteinToolkit [39,40] infrastructure. We use the Carpet mesh refinement driver to provide a "moving boxes" style of mesh refinement [41]. Fifth-order Kreiss-Oliger dissipation is added to evolved variables with dissipation coefficient $\epsilon = 0.1$. For the CCZ4 damping parameters, we chose $\kappa_1 = 0.2$, $\kappa_2 = 0$, and $\kappa_3 = 0$ (see [34]), but found that these had to be modified during the evolution.

We locate the apparent horizons using the AHFinderDirect code [42] and measure the horizon spins using the isolated horizon (IH) algorithm [43]. We calculate the radiation scalar ψ_4 using the Antenna thorn [44,45]. We then extrapolate the waveform to an infinite observer location using the perturbative formulas given in Ref. [46].

For the gauge equations, we use [2,47,48]

$$(\partial_t - \beta^i \partial_i)\alpha = -2\alpha^2 K, \tag{15a}$$

$$\partial_t \beta^a = \frac{3}{4}\tilde{\Gamma}^a - \eta\beta^a. \tag{15b}$$

Note that the lapse is not evolved with the standard $1 + \log$ form. Here we multiply the rhs of the lapse equation by an additional factor of α. This has the effect of increasing the equilibrium (coordinate) size of the horizons. For the initial
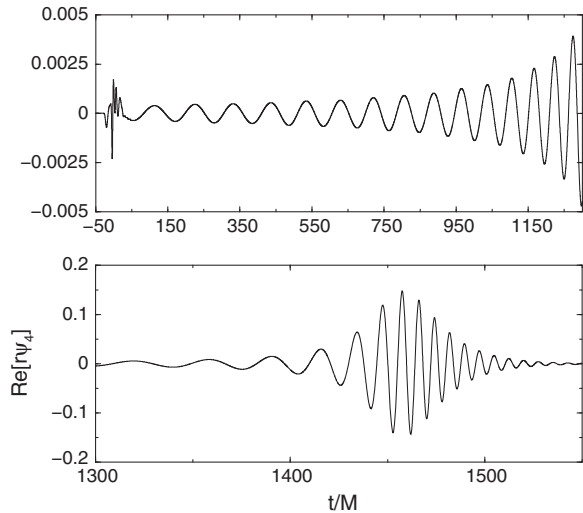
FIG. 1. The HɪSPID waveform showing the amplitude of the initial data pulse compared to the physical waveform. Note how little the pulse contaminates the rest of the signal.

values of shift, we chose $\beta^i(t = 0) = 0$, while for the initial values of the lapse, we chose an ad-hoc function $\alpha(t = 0) = \tilde{\psi}^{-2}$, where $\tilde{\psi} = 1 + \mathcal{M}/(2r_1) + \mathcal{M}/(2r_2)$ and r_i is the coordinate distance to BH i. For the function η, we chose

$$\eta(\vec{r}) = (\eta_c - \eta_o) \exp(-(r/\eta_s)^4) + \eta_o, \qquad (16)$$

where $\eta_c = 2.0/M$, $\eta_s = 40.0M$, and $\eta_o = 0.25/M$. With this choice, η is small in the outer zones. As shown in Ref. [49], the magnitude of η limits how large the time step can be with $dt_{\max} \propto 1/\eta$. Since this limit is independent of spatial resolution, it is only significant in the very coarse outer zones where the standard Courant-Friedrichs-Lewy condition would otherwise lead to a large value for $dt_{\max}$.

We evolved the $\chi = 0.99$ data using 11 levels of refinement, with the outermost grid extending to $400M$ with a grid spacing of $2.78M$. The grid spacing on the finest grid was $h = M/368.64$. The total cost of the simulation was 710 KSU.

One remarkable consequence of these superimposed Kerr data is how small the initial pulse of unphysical radiation is. As first seen in the nonboosted case by Hannam *et al.* [26], the initial pulse is roughly 4 times as large as the orbital signal at a separation of $D = 10M$. While this may sound quite large, for a $\chi = 0.9$ binary, the amount of unphysical radiation for a Bowen-York binary is 6 times more, and it rapidly increases with spin. The full waveform, including initial pulse, is shown in Fig. 1.

III. RESULTS

We performed a single simulation from a coordinate separation of $10M$ (proper separation of $12.2M$) through merger for an equal-mass binary where both spins are aligned with the orbital angular momentum and have

dimensionless magnitudes of 0.99. We compare these with the BBH:0177 waveform [17,50]. In order to compare the HɪSPID and SXS waveform, we rescale the time coordinate by the ratio of the final masses and then introduce a constant phase and time translation to minimize the RMS difference between the two waveforms. We note that the SXS waveform is longer by about $t = 5000M$.

In Figs. 2 and 3, we directly compare the new HɪSPID waveform with the corresponding SXS waveform. We translate the HɪSPID waveform to maximize the overlap. Hence, the "starting" time in the figures is $t \sim 5000M$. The overlap is defined by [51]

$$\underset{t_0}{\text{MAX}} \frac{|\langle R(t), S(t + t_0)\rangle|}{\sqrt{|\langle R(t), R(t)\rangle||\langle S(t + t_0), S(t + t_0)\rangle|}}, \qquad (17)$$

where

$$\langle a(t), b(t)\rangle = \int_0^{t_f} \bar{a}(t) b(t) dt, \qquad (18)$$

an overbar denotes complex conjugation, and t_0 is chosen to maximize the result, while $t = 0$ corresponds to the time just after the initial pulse has radiated away and t_f to the last time step in the HɪSPID simulation. We find an overlap of 0.99975 for the ($\ell = 2$, $m = 2$) mode, which is quite good considering that the HɪSPID waveform is eccentric ($e \sim 0.01$), while the SXS waveform is not. Note the phase agreement is within 0.25 rad across the entire waveform and the amplitude agreement is better than 4%. The agreement in frequency is even better, with a relative difference of lass than 2% across the entire waveform.

The next largest modes after the ($\ell = 2$, $m = \pm 2$) modes are the ($\ell = 4$, $m = \pm 4$) modes. However, in our simulations, these show significant effects of dissipation postmerger. We, therefore, compare the ($\ell = 3$, $m = 2$) mode instead. As shown in Fig. 4, the agreement between HɪSPID and SXS is quite good even for a higher-order mode. The overlap between the ($\ell = 3$, $m = 2$) modes is 0.998 [the constant t_0 was fixed by maximizing the overlap of the ($\ell = 2$, $m = 2$) modes, the maximum overlap of the ($\ell = 3$, $m = 2$) is 0.9998].

A. Diagnostics

One of the most important diagnostics for a BHB simulation is the degree to which the constraints are satisfied and to what degree the horizon masses and spins are conserved. In Fig. 5, we show the individual horizon mass and (dimensionless spin). Note that prior to merger, the spins are within ± 0.001 of 0.99 and the masses change by less than 0.2%. In Fig. 6, we show the L^2 norm of the Hamiltonian and momentum constraints. Here the L^2 norm is over the region outside the two horizons (or common horizon) and inside a sphere of radius $30M$. Note how the constraints start small (10^{-8}) and quickly increase to 10^{-4}.
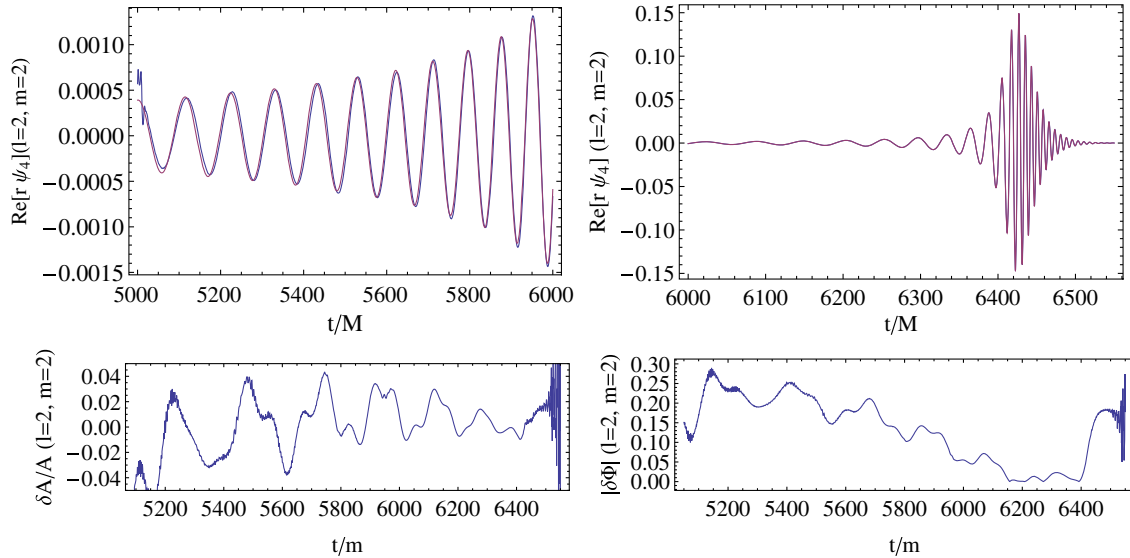
FIG. 2.   (Top left and top right) The new HıSpID simulation (blue) and the SXS simulation (red) of the ($\ell = 2$, $m = 2$) mode of ψ_4 (real part). The HıSpID waveform was translated by $t \sim 5000M$. (Bottom left) The difference in amplitude between the HıSpID and SXS waveforms. (Bottom right) The difference in phase between the HıSpID and SXS waveforms. Note that the period of oscillations in $\delta A/A$ and $\delta \Phi$ is very close to the orbital timescale (see Fig. 7). This indicates that these oscillations are likely due to eccentricity.
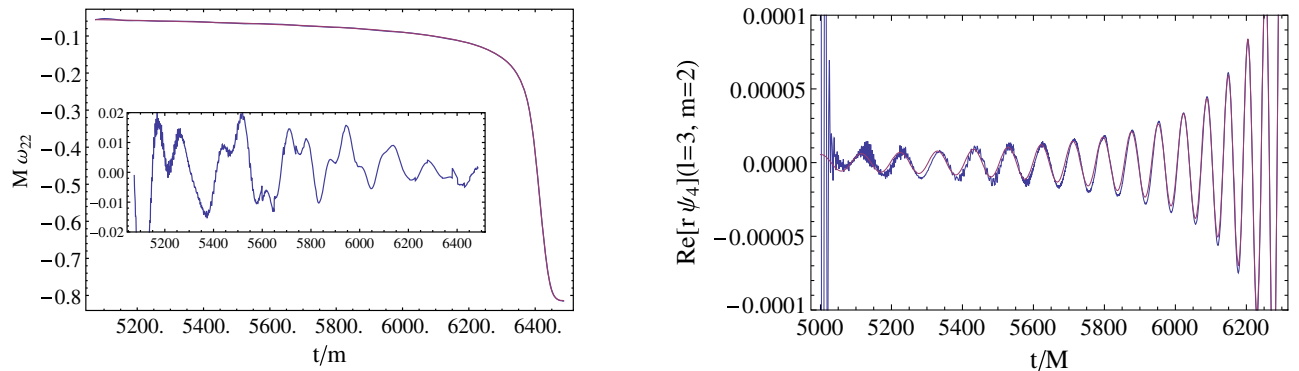
FIG. 3.   The frequency of the ($\ell = 2$, $m = 2$) mode of ψ_4 for the HıSpID (blue) and SXS (red) waveforms. The inset shows the relative differences in frequency between the two waveforms.

This increase is due to unresolved features in the initial data (i.e., the AMR grid cannot propagate high-frequency data accurately). The constraints then damp, as is expected for CCZ4. However, they start to exponentially blow up around $400M$. We found that the parameters κ_1 and κ_2 had to be fine-tuned to prevent this blow-up. We found that increasing the damping parameters can effectively drive the constraints smaller for a short time, but large values of κ_i led to an exponential blowup of the constraints at later times. We used a trial-and-error approach to fine-tuning these parameters during the run. We show the values of κ_1 used during the evolution in the top of Fig. 6.

One challenge with the HıSpID data is obtaining low-eccentricity data without performing an iterative procedure where the initial data are evolved for a few orbits and then refined based on the measured orbital evolution [52–55].
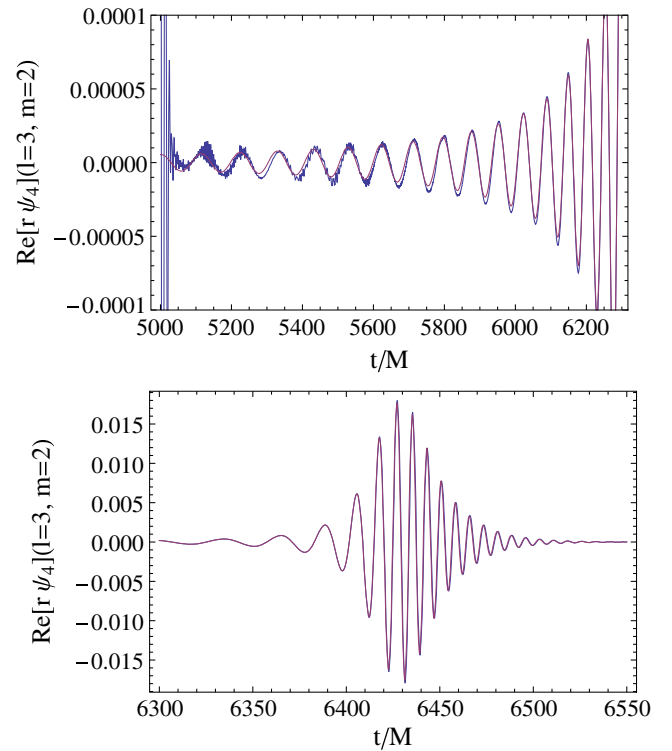

FIG. 4.   The new HıSpID simulation (blue) and the SXS simulation (red) of the ($\ell = 3$, $m = 2$) mode of ψ_4 (real part). The HıSpID waveform was translated by $t \sim 5000M$.

In [32], it was shown that relatively low-eccentricity initial data parameters can be obtained using higher-order post-Newtonian approximations. However, as shown in Table I, unlike for Bowen-York data, here we cannot specify the
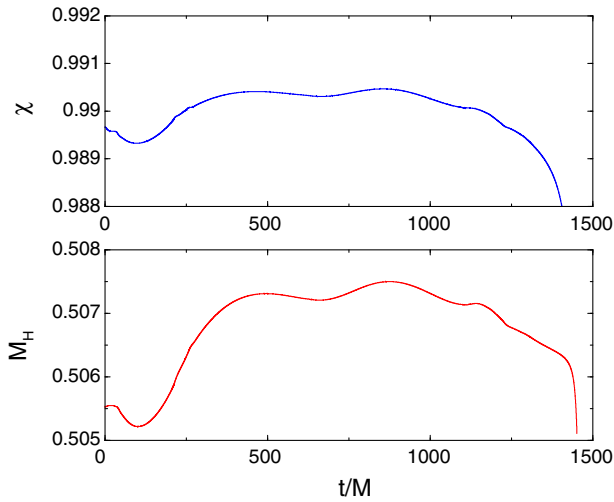
FIG. 5.   The dimensionless spin (top) and horizon (Christodoulou) mass (bottom) for the two horizons in the binary.
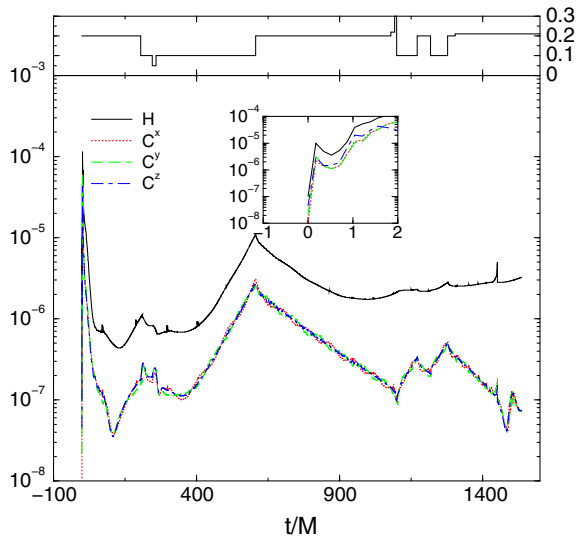

FIG. 6. L^2 norm of the Hamiltonian and momentum constraints versus time. Note the rapid growth during the first 2M of evolution. The CCZ4 damping parameters $\kappa_{1,2}$ were adjusted during the evolution to suppress the constraint growths apparent at $t = 400M$–$600M$, and again at $t = 900M$. The top panel shows the value of κ_1 used during the simulation.

initial momenta precisely. That is to say, the orbital angular momentum of the background (i.e., prior to the inclusion of corrections due to the fields u and b^i) is significantly larger than the final orbital angular momentum of the initial data. We compensate for this by increasing the momentum parameters until the ADM angular momentum matches the expected value based on quasicircular orbits. However, we have no method of correcting for the radial momentum (other than using an iterative evolution procedure). Consequentially, the eccentricity of the initial data is relatively high at $e \approx 0.01$, as shown in Fig. 7. Of course,
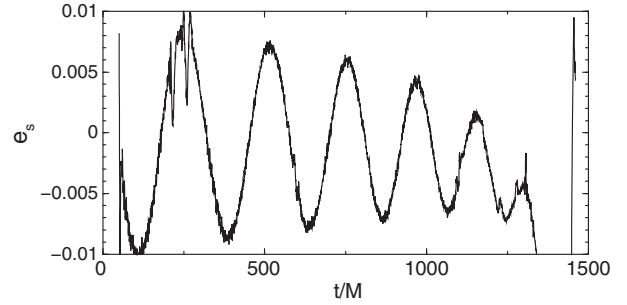

FIG. 7.   The eccentricity of the HISPID UU99 simulation as measured using the approximation $e_s \approx s^2 \ddot{s}$, where s is the proper distance of the part of the coordinate line segment connecting the centroids of the two black holes that is outside both horizons.
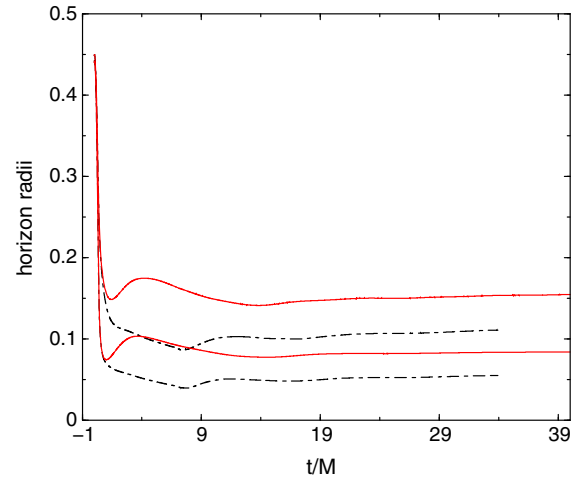

FIG. 8.   The coordinate radii (minimum and maximum) versus time for the standard $1 + \log$ lapse (dot-dashed curves) and the modified lapse condition used for the full simulation. Note that in both gauges there is an extremely rapid evolution of the horizon size and shape during the first few M of evolution. The new gauge produces a horizon that is $\approx 8/5$ times larger.

we can run the data for a few orbits and then refine the parameters, but such a procedure is computationally expensive. We are thus working on improving the evolution efficiency.

One method which we found was useful for increasing the run speed was to change the lapse condition. When using the standard $1 + \log$ lapse, the horizons are a factor of 0.625 as wide (see Fig. 8). Evolving the data with horizons this small requires roughly a factor of 2 more in terms of computational expense because an additional level of refinement is needed. Using harmonic slicing leads to still larger horizons, but this proved to be unstable. The rapid change in the gauge at early time, as is evident in the size and shape of the horizon (see Fig. 8) may be responsible for the initial jump in the constraint violations seen in Fig. 6.

IV. DISCUSSION

In this paper, we demonstrated that it is possible to evolve black hole binaries with nearly maximal spin using the "moving puncture" formalism. This means that comparative studies of these challenging evolutions by the two main methods (the generalized harmonic approach used by SXS and various flavors of the "moving punctures" approach used by many other groups) to numerically solve the field equations of general relativity field equations can now be performed. Independent comparison, along the lines explored in [56], have been very successful in demonstrating the accuracy and correctness of moderate-spin black hole simulations. These new techniques also open the possibility to explore a region of parameter space which is of high interest for both astrophysical and gravitational wave studies.

ACKNOWLEDGMENTS

[1] F. Pretorius, Phys. Rev. Lett. **95**, 121101 (2005).
[2] M. Campanelli, C. O. Lousto, P. Marronetti, and Y. Zlochower, Phys. Rev. Lett. **96**, 111101 (2006).
[3] J. G. Baker, J. Centrella, D.-I. Choi, M. Koppitz, and J. van Meter, Phys. Rev. Lett. **96**, 111102 (2006).
[4] J. A. Gonzalez, U. Sperhake, and B. Brugmann, Phys. Rev. D **79**, 124006 (2009).
[5] C. O. Lousto, H. Nakano, Y. Zlochower, and M. Campanelli, Phys. Rev. D **82**, 104057 (2010).
[6] C. O. Lousto and Y. Zlochower, Phys. Rev. Lett. **106**, 041101 (2011).
[7] U. Sperhake, V. Cardoso, C. D. Ott, E. Schnetter, and H. Witek, Phys. Rev. D **84**, 084038 (2011).
[8] T. Chu, H. Fong, P. Kumar, H. P. Pfeiffer, M. Boyle, D. A. Hemberger, L. E. Kidder, M. A. Scheel, and B. Szilagyi, Classical Quantum Gravity **33**, 165001 (2016).
[9] K. Jani, J. Healy, J. A. Clark, L. London, P. Laguna, and D. Shoemaker, Classical Quantum Gravity **33**, 204001 (2016).
[10] G. Lovelace, R. Owen, H. P. Pfeiffer, and T. Chu, Phys. Rev. D **78**, 084017 (2008).
[11] https://www.black-holes.org.
[12] G. B. Cook and J. W. York, Jr., Phys. Rev. D **41**, 1077 (1990).
[13] J. M. Bowen and J. W. York, Jr., Phys. Rev. D **21**, 2047 (1980).
[14] S. Dain, C. O. Lousto, and R. Takahashi, Phys. Rev. D **65**, 104038 (2002).
[15] C. O. Lousto, H. Nakano, Y. Zlochower, B. C. Mundim, and M. Campanelli, Phys. Rev. D **85**, 124013 (2012).
[16] G. Lovelace, M. Boyle, M. A. Scheel, and B. Szilagyi, Classical Quantum Gravity **29**, 045003 (2012).
[17] M. A. Scheel, M. Giesler, D. A. Hemberger, G. Lovelace, K. Kuper, M. Boyle, B. Szilágyi, and L. E. Kidder, Classical Quantum Gravity **32**, 105009 (2015).
[18] H. Yang, A. Zimmerman, and L. Lehner, Phys. Rev. Lett. **114**, 081101 (2015).
[19] J. D. Schnittman, Phys. Rev. Lett. **113**, 261102 (2014).

[20] E. Berti, R. Brito, and V. Cardoso, Phys. Rev. Lett. **114**, 251103 (2015).
[21] C. M. Hirata, Phys. Rev. D **83**, 104024 (2011).
[22] M. van de Meent, Phys. Rev. D **90**, 044027 (2014).
[23] B. P. Abbott et al. (Virgo and LIGO Scientific Collaboration), Phys. Rev. D **94**, 064035 (2016).
[24] I. Ruchlin, J. Healy, C. O. Lousto, and Y. Zlochower, Phys. Rev. D **95**, 024033 (2017).
[25] J. Healy, I. Ruchlin, C. O. Lousto, and Y. Zlochower, Phys. Rev. D **94**, 104020 (2016).
[26] M. Hannam, S. Husa, B. Bruegmann, J. A. Gonzalez, and U. Sperhake, Classical Quantum Gravity **24**, S15 (2007).
[27] J. W. York, Phys. Rev. Lett. **82**, 1350 (1999).
[28] G. B. Cook, Living Rev. Relativ. **3**, 5 (2000).
[29] H. P. Pfeiffer and J. W. York, Phys. Rev. D **67**, 044022 (2003).
[30] M. Alcubierre, Introduction to 3+1 Numerical Relativity (Oxford University Press, New York, 2008).
[31] M. Ansorg, B. Brügmann, and W. Tichy, Phys. Rev. D **70**, 064011 (2004).
[32] J. Healy, C. O. Lousto, H. Nakano, and Y. Zlochower, Classical Quantum Gravity **34**, 145011 (2017).
[33] Y. Zlochower, J. G. Baker, M. Campanelli, and C. O. Lousto, Phys. Rev. D **72**, 024021 (2005).
[34] D. Alic, C. Bona-Casas, C. Bona, L. Rezzolla, and C. Palenzuela, Phys. Rev. D **85**, 064040 (2012).
[35] T. Nakamura, K. Oohara, and Y. Kojima, Prog. Theor. Phys. Suppl. **90**, 1 (1987).
[36] M. Shibata and T. Nakamura, Phys. Rev. D **52**, 5428 (1995).
[37] T. W. Baumgarte and S. L. Shapiro, Phys. Rev. D **59**, 024007 (1998).
[38] C. O. Lousto and Y. Zlochower, Phys. Rev. D **77**, 024034 (2008).
[39] Cactus Computational Toolkit home page, http://cactuscode.org.
[40] Einstein Toolkit home page, http://einsteintoolkit.org.

[41] E. Schnetter, S. H. Hawley, and I. Hawke, Classical Quantum Gravity **21**, 1465 (2004).

[42] J. Thornburg, Classical Quantum Gravity **21**, 743 (2004).

[43] O. Dreyer, B. Krishnan, D. Shoemaker, and E. Schnetter, Phys. Rev. D **67**, 024018 (2003).

[44] M. Campanelli, B. J. Kelly, and C. O. Lousto, Phys. Rev. D **73**, 064005 (2006).

[45] J. G. Baker, M. Campanelli, and C. O. Lousto, Phys. Rev. D **65**, 044001 (2002).

[46] H. Nakano, J. Healy, C. O. Lousto, and Y. Zlochower, Phys. Rev. D **91**, 104022 (2015).

[47] M. Alcubierre, B. Brügmann, P. Diener, M. Koppitz, D. Pollney, E. Seidel, and R. Takahashi, Phys. Rev. D **67**, 084023 (2003).

[48] J. R. van Meter, J. G. Baker, M. Koppitz, and D.-I. Choi, Phys. Rev. D **73**, 124011 (2006).

[49] E. Schnetter, Classical Quantum Gravity **27**, 167001 (2010).

[50] http://www.black-holes.org/waveforms.

[51] M. Campanelli, C. O. Lousto, H. Nakano, and Y. Zlochower, Phys. Rev. D **79**, 084010 (2009).

[52] H. P. Pfeiffer, D. A. Brown, L. E. Kidder, L. Lindblom, G. Lovelace, and M. A. Scheel, Classical Quantum Gravity **24**, S59 (2007).

[53] A. Buonanno, L. E. Kidder, A. H. Mroue, H. P. Pfeiffer, and A. Taracchini, Phys. Rev. D **83**, 104034 (2011).

[54] M. Purrer, S. Husa, and M. Hannam, Phys. Rev. D **85**, 124051 (2012).

[55] L. T. Buchman, H. P. Pfeiffer, M. A. Scheel, and B. Szilagyi, Phys. Rev. D **86**, 084033 (2012).

[56] G. Lovelace *et al.*, Classical Quantum Gravity **33**, 244002 (2016).